Micro-Modeling of Porous Composite Anodes for Solid Oxide Fuel Cells

Siamak Farhad and Feridun Hamdullahpur
Dept. of Mechanical and Mechatronics Engineering, University of Waterloo, Waterloo, ON, Canada N2L 3G1

DOI 10.1002/aic.12689
Published online June 24, 2011 in Wiley Online Library (wileyonlinelibrary.com).

A new anode micromodel for solid oxide fuel cells to predict the electrochemical performance of hydrocarbon-fuelled porous composite anodes with various microstructures is developed. In this model, the random packing sphere method is used to estimate the anode microstructural properties, and the complex interdependency among the multicomponent mass transport, electron and ion transports, and electrochemical and chemical reactions is taken into account. As a case study, a porous Ni–YSZ composite anode operated with biogas fuel is simulated numerically and distributions of the current density, polarization, and mole fraction and rate of flux of the fuel components along the thickness of the anode are determined. The effect of the anode microstructural variables including the porosity, thickness, particle-size ratio, and particle size and volume fraction of Ni particles on the anode electrochemical performance is also studied. © 2011 American Institute of Chemical Engineers *AIChE J,* 58: 1893–1906, 2012
Keywords: micromodeling, microstructure of porous composite anode, electrochemical performance, solid oxide fuel cell, biogas

Introduction

The microstructure of porous composite anodes in solid oxide fuel cells (SOFCs) is made of three phases of electron conducting particles to transport electrons, ion conducting particles to transport oxygen ions, and pores to transport reactant gases. As the electrochemical reactions take place at the active sites of the anode, where these three phases are present, the anode microstructural characteristics can affect significantly the anode electrochemical performance. In fact, the microstructure of the anode affects the activation polarization due to the change of the active sites for electrochemical reactions, the ohmic polarization due to the change of the effective resistivities of electron and ion conductors, and the concentration polarization due to the change of the anode pore size. Therefore, to fabricate a porous composite anode with a high-electrochemical performance, the effect of all the anode microstructural variables on the electrochemical performance should be determined.

Some experimental studies[1–5] investigated the effect of the microstructure of porous composite anodes on their electrochemical performance. However, these studies are generally limited to a small number of anode samples tested at some specific operating conditions and cannot be used to fabricate an anode with a high-electrochemical performance. The anode micromodels cited in the literature are also mostly limited to hydrogen fuel,[6–10] because the effect of the multicomponent mass transfer (at least for a complex system of fuel mixture containing CH_4, H_2, CO, H_2O, CO_2, and N_2) and carbon monoxide electrochemical reaction was not considered in the concentration and activation polarizations, respectively. In this study, the complex interdependency among the multicomponent mass transport, electron and ion transports, and the chemical and electrochemical reactions in porous composite anodes is taken into account and a comprehensive micromodel to predict the electrochemical performance of porous composite anodes with various microstructures and operated with an arbitrary fuel containing CH_4, H_2, CO, H_2O, CO_2, and N_2, is developed. As a case

Correspondence concerning this article should be addressed to F. Hamdullahpur at fhamdull@uwaterloo.ca.

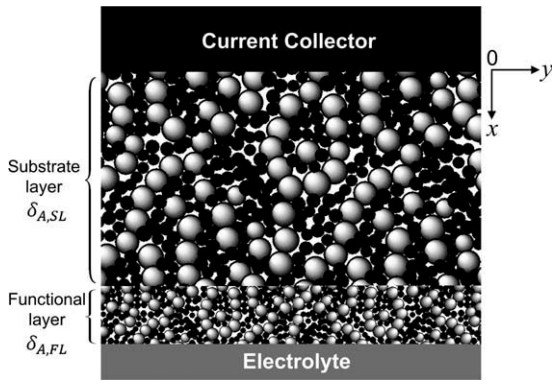

Figure 1. Schematic of a two-layer porous composite anode.

study, a biogas-fuelled porous Ni–YSZ (yttria-stabilized zirconia) anode with two substrate and functional layers is studied through computer simulation; and the distribution of the current density, polarization, and mole fraction and rate of flux of the fuel along the thickness of the anode is determined. Then, the effect of the anode microstructural variables including the porosity, thickness, particle-size ratio, and particle size and volume fraction of Ni particles on the anode total resistance is investigated. Using this model, in addition to the anode total resistance, the power density, which is essential for portable applications of SOFCs,[11] and the exergy destruction[12,13] can be considered to study the anode electrochemical performance.

Micromodeling

To predict the effect of the anode microstructure on its electrochemical performance, a detailed micromodel is required. The micromodel starts with the anode microstructure modeling through which the anode microstructural properties including the electrochemical active area per unit volume, permeability, average size of pores, tortuosity, and effective resistivity of electron and ion conductors are determined from the microstructural variables. Different methods with various degrees of complexity are cited in the literature for the microstructure modeling.[14–18] Among them, we select the random packing sphere method because of its simplicity and low-computational cost, even for small size particles. This method is applicable for electrodes that their particles remain almost spherical during the sintering process; and loses its validity when the contact angle between particles is large. Several researchers reported that the average contact angle would be almost 30° after the sintering of SOFC's electrodes[8–10]; hence, the anode can be assumed to be a random packing of spheres. Furthermore, in this method, both electron and ion conductors are assumed monosized particles and the particle coordination number and percolation theories are used to estimate the anode microstructural properties. The procedure of estimating microstructural properties through this method is described in detained in another article of the authors.[19]

After the estimation of microstructural properties, the micromodel is developed. The micromodel of the porous composite anode developed in this study is a steady-state one-dimensional model along the thickness of the anode (x-axis in Figure 1). It is assumed that the gaseous fuel is treated as an ideal gas, the temperature of the anode is uniform, and the water gas shift (WSG) reaction R1 is locally in equilibrium. This assumption is introduced, because the WSG reaction is very fast compared with the H_2 and CO electrochemical reactions at high-operating temperature of SOFCs, especially in the presence of catalytic effect of Ni particles in anode. We also assumed that the methane content of the fuel participate neither in electrochemical nor steam reforming reactions inside the microstructure of the anode.

$$CO + H_2O \rightleftarrows CO_2 + H_2 \qquad (R1)$$

As shown in Figure 1, the anode studied is made of a thick substrate layer with thickness of $\delta_{A,SL}$, as a mechanical support of the cell structure, and a thin functional layer with thickness of $\delta_{A,FL}$ for H_2 and CO electrochemical reactions. As these two layers are different operationally, we model them separately.

Micromodeling of the substrate layer

In the anode substrate layer ($0 \le x \le \delta_{A,SL}$), H_2 and CO molecules are transferred from the bulk fuel stream to the anode functional layer and H_2O and CO_2 molecules are transferred from the anode functional layer to the bulk fuel stream through pores. The electrons are also transferred from the anode functional layer to the interconnect through the percolated Ni particles in the substrate layer. As the partial pressure of the fuel components changes along the anode substrate layer and the WGS reaction should be locally maintained in equilibrium, a conversion of CO to H_2, or vice versa, through WGS reaction R1 may occur in this layer. As the effect of the transport of electron on the electrochemical performance of anode is negligible, this effect is not considered in the micromodel of the substrate layer.

The micromodel of the substrate layer is required to determine the partial pressure and rate of flux of the gaseous fuel components at the interface of the substrate and functional layers. For this purpose, the dusty gas model (DGM) as a model that can take into account the combined effect of the gas transport through porous media[20–24] is used to establish a relation between the local partial pressures and rate of fluxes of the fuel components.

In the absence of thermal, forced, and surface diffusions, the gas transport through the porous anode can be described by three mechanisms of the ordinary diffusion, in which the different components of the gaseous fuel move relative to each other under the influence of concentration gradients; Knudsen diffusion, in which the mean free path of molecules of different components of the gaseous fuel is in the order of the pore size and the gas molecules collide frequently with the pore walls; and viscous flow, in which the gaseous fuel acts as a continuum fluid driven by a pressure gradient through pores of the anode. The electrical analogy for combined mechanisms of the ordinary diffusion, Knudsen diffusion and viscous flow is shown in Figure 2. As seen, to determine the total flux, Knudsen and ordinary diffusive

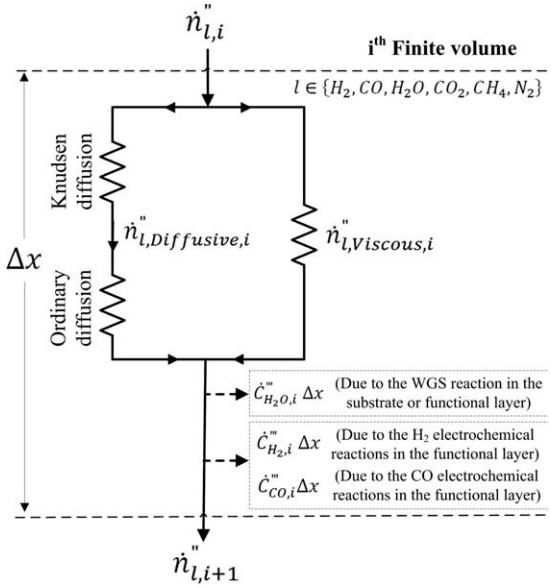

Figure 2. The electrical analogy for combined mechanisms of gas transport in the porous composite anode.

flows are combined like resistors in series, and the total diffusive flow is combined with the viscous flow like resistors in parallel

$$\dot{n}''_l(x) = \dot{n}''_{l,\text{diffusion}}(x) + \dot{n}''_{l,\text{viscous}}(x) \tag{1}$$

The DGM for the total diffusive flow, including the Maxwell–Stefan equation for the multicomponent ordinary and Knudsen diffusions, is expressed as[20]

$$\frac{dp_l(x)}{dx} = -\frac{R_u T_s}{p_F(x)} \sum_{m=1}^{n} \frac{p_m(x)\dot{n}''_{l,\text{diffusion}}(x) - p_l(x)\dot{n}''_{m,\text{diffusion}}(x)}{D^{\text{eff}}_{l-m}} - R_u T_s \frac{\dot{n}''_{l,\text{diffusion}}(x)}{D^{\text{eff}}_{K,l}}, l \in \{H_2, CO, H_2O, CO_2, CH_4, N_2\} \tag{2}$$

The effective ordinary and Knudsen diffusion coefficients are estimated from Eqs. 3[25] and 4,[26] respectively. It is noted that the atomic diffusion volume, V_a, of H_2, CO, H_2O, CO_2, CH_4, and N_2 in Eq. 3 is 6.12, 18.0, 13.1, 26.7, 25.14, and 18.5 cm^3, respectively.[25]

$$D^{\text{eff}}_{l-m} = \frac{0.0101325}{\left(V^{1/3}_{a,l} + V^{1/3}_{a,m}\right)^2} \left(\frac{1}{MW_l} + \frac{1}{MW_m}\right)^{0.5} \frac{T^{1.75}_s}{p_F(x)} \left(\frac{\varepsilon_A}{\tau_A}\right) \tag{3}$$

$$D^{\text{eff}}_{K,l} = 48.5\, d_{\text{pores}} \sqrt{\frac{T_s}{MW_l}} \left(\frac{\varepsilon_A}{\tau_A}\right) \tag{4}$$

The behavior of viscous flow in the porous anode is mathematically described as the creeping flow at which the Reynolds number is very small, such that the inertia effects can be ignored in comparison to the viscous effects. If the gas mixture is not accelerating, the net force on any finite volume of the anode in x direction is zero, so the viscous-drag force just balances the force because of the pressure difference across the finite volume. In this condition, the rate of flux corresponding to viscous flow through porous anode can be described by Darcy law as follows

$$\dot{n}''_{l,\text{viscous}}(x) = -\frac{p_l(x)}{R_u T_s} \frac{\beta_0}{\mu(x)} \frac{dp_F(x)}{dx} \tag{5}$$

The permeability of the porous anode, β_0, can be estimated from the Carman–Kozeny correlation for a porous medium made of spherical particles. Of course, we modified this correlation for the random mixture of binary spherical particles as follows

$$\beta_0 = \frac{1}{180} \frac{\varepsilon^3_A}{(1-\varepsilon_A)^2} \left(\frac{\varphi_{Ni}}{d_{Ni}} + \frac{1-\varphi_{Ni}}{d_{YSZ}}\right)^{-2} \tag{6}$$

We also estimated the dynamic viscousity of fuel, as an n-component gas mixture, using the Reichenberg method from the dynamic viscousity of the pure components.[27]

If the rate of flux corresponding to viscous flow in Eq. 5 is substituted into Eq. 1 and the rate of flux corresponding to the diffusive flow is obtained from Eq. 1 and substituted into Eq. 2, the multicomponent gas transport in the porous anode on the basis of the DGM for the combined mechanisms of the ordinary diffusion, Knudsen diffusion and viscous flow is obtained as follows

$$\frac{dp_l(x)}{dx} = -\frac{R_u T_s}{p_F(x)} \sum_{m=1}^{n} \frac{p_m(x)\dot{n}''_l(x) - p_l(x)\dot{n}''_m(x)}{D^{\text{eff}}_{l-m}} - R_u T_s \frac{\dot{n}''_l(x)}{D^{\text{eff}}_{K,l}} - \frac{\beta_0 p_l(x)}{D^{\text{eff}}_{K,l}\,\mu(x)} \frac{dp_F(x)}{dx} \tag{7}$$

By developing this equation for all components of the fuel and adding both sides of the equations obtained, the change of the fuel pressure along the thickness of the anode is determined as

$$\frac{dp_F(x)}{dx} = -R_u T_s \frac{\sum_{m=1}^{n} \dot{n}''_m(x)/D^{\text{eff}}_{K,m}}{\left(1 + \frac{\beta_0}{\mu(x)} \sum_{m=1}^{n} \frac{p_m(x)}{D^{\text{eff}}_{K,m}}\right)} \tag{8}$$

Substituting Eq. 8 into Eq. 7 yields

$$\frac{dp_l(x)}{dx} = -\frac{R_u T_s}{\sum_{m=1}^{n} p_m(x)} \sum_{m=1}^{n} \frac{p_m(x)\dot{n}''_l(x) - p_l(x)\dot{n}''_m(x)}{D^{\text{eff}}_{l-m}} - R_u T_s \frac{\dot{n}''_l(x)}{D^{\text{eff}}_{K,l}} + R_u T_s \frac{\beta_0 p_l(x)}{D^{\text{eff}}_{K,l}\mu(x)} \times \frac{\sum_{m=1}^{n} \dot{n}''_m(x)/D^{\text{eff}}_{K,m}}{\left(1 + \frac{\beta_0}{\mu(x)} \sum_{m=1}^{n} \frac{p_m(x)}{D^{\text{eff}}_{K,m}}\right)}, \quad l \in \{H_2, CO, H_2O, CO_2, CH_4, N_2\} \tag{9}$$

In this equation, the gradient of the local partial pressure is dependent on the local rate of flux of the fuel components. The rate of flux of nitrogen and methane are zero in the anode microstructure; the local rate of flux of water and carbon dioxide is equal in magnitude and opposite in direction to

that of hydrogen and carbon monoxide, respectively; and the local rate of flux of hydrogen and carbon monoxide can be obtained from the mass conservation equation as follows

$$\frac{d\dot{n}''_{H_2}(x)}{dx} = \dot{C}'''_{H_2O,WGS}(x) \tag{10}$$

$$\dot{n}''_{CO}(x) = \frac{i_{tot}}{2F} - \dot{n}''_{H_2}(x) \tag{11}$$

$$\dot{n}''_{H_2O}(x) = -\dot{n}''_{H_2}(x) \tag{12}$$

$$\dot{n}''_{CO_2}(x) = -\dot{n}''_{CO}(x) \tag{13}$$

The rate of flux of hydrogen in Eq. 10 is dependent on the rate of water consumption through WGS reaction R1, $\dot{C}'''_{H_2O,WGS}(x)$, in the anode substrate layer. The rate of water consumption through WGS reaction can be determined from the relation of the equilibrium constant of the WGS reaction with H_2, CO, H_2O, and CO_2 partial pressures

$$K_{p,WGS}(T_s) = \exp\left(-\frac{g^o_{CO_2}(T_s) + g^o_{H_2}(T_s) - g^o_{CO}(T_s) - g^o_{H_2O}(T_s)}{R_u T_s}\right) = \frac{C_{H_2}(x)C_{CO_2}(x)}{C_{H_2O}(x)C_{CO}(x)} = \frac{p_{H_2}(x)p_{CO_2}(x)}{p_{H_2O}(x)p_{CO}(x)} \tag{14}$$

Therefore, the partial pressure and rate of flux of the fuel components are coupled and the system of Eqs. 15 with the associated boundary conditions should be solved to determine these variables along the anode substrate layer.

$$\begin{cases} \frac{dp_l(x)}{dx} = \frac{-R_u T_s}{\sum_{m=1}^{n} p_m(x)} \sum_{m=1}^{n} \frac{p_m(x)\dot{n}''_l(x) - p_l(x)\dot{n}''_m(x)}{D^{eff}_{l-m}} - R_u T_s \frac{\dot{n}''_l(x)}{D_{K,l}} + R_u T_s \frac{\beta_0 p_l(x)}{D^{eff}_{K,l}\mu(x)} \\ \qquad \frac{\sum_{m=1}^{n} \dot{n}''_m(x)/D^{eff}_{K,m}}{\left(1 + \frac{\beta_0}{\mu(x)} \sum_{m=1}^{n} \frac{p_m(x)}{D^{eff}_{K,m}}\right)}, l \in \{H_2, CO, H_2O, CO_2, CH_4, N_2\} \\ \frac{d\dot{n}''_{H_2}(x)}{dx} = \dot{C}'''_{H_2O,WGS}(x) \\ \dot{n}''_{CO}(x) = \frac{i_{tot}}{2F} - \dot{n}''_{H_2}(x) \\ \dot{n}''_{H_2O}(x) = -\dot{n}''_{H_2}(x) \\ \dot{n}''_{CO_2}(x) = -\dot{n}''_{CO}(x) \\ \dot{n}''_{CH_4}(x) = \dot{n}''_{N_2}(x) = 0 \\ K_{p,WGS}(T_s) = \frac{p_{H_2}(x)p_{CO_2}(x)}{p_{H_2O}(x)p_{CO}(x)} \end{cases}$$

$$\text{At } x = 0: p_l = p_l(0), l \in \{H_2, CO, H_2O, CO_2, CH_4, N_2\} \tag{15}$$

Micromodeling of the functional layer

In the anode functional layer ($\delta_{A,SL} \le x \le \delta_A$), oxygen ions are transferred from the electrolyte to reaction sites through the percolated YSZ particles, H_2 and CO molecules are transferred from the anode substrate layer to the reaction sites of the functional layer through pores, H_2 and CO electrochemical reactions R2 and R3 take place at the reaction sites, electrons produced are transferred from the reaction sites to the anode substrate layer through the percolated Ni particles, and H_2O and CO_2 molecules produced are transferred from reaction sites to the anode substrate layer through pores. As the partial pressure of the fuel components changes along the anode functional layer and the WGS reaction should be locally maintained in equilibrium, a conversion of CO to H_2, or vice versa, through WGS reaction R1 may occur in this layer.

$$H_2 + O^{2-} \underset{k_{b,H_2}}{\overset{k_{f,H_2}}{\rightleftarrows}} H_2O + 2e^- \tag{R2}$$

$$CO + O^{2-} \underset{k_{b,CO}}{\overset{k_{f,CO}}{\rightleftarrows}} CO_2 + 2e^- \tag{R3}$$

As the ion conductivity of Ni and electron conductivity of YSZ are negligible, the electron and ion local current densities generated from the electrochemical reactions R2 and R3 can be obtained on the basis of Kirchhoff's circuit law from the following equations[7]

$$\frac{di_{Ni}(x)}{dx} = -A_{TPB} i_n(x) \qquad i_{Ni}(\delta_{A,SL}) = i_{tot} \tag{16}$$

$$\frac{di_{YSZ}(x)}{dx} = A_{TPB} i_n(x) \qquad i_{YSZ}(\delta_{A,SL}) = 0 \tag{17}$$

To solve these differential equations, the anode total transfer current density per unit of electrochemical active area, $i_n(x)$, due to the electrochemical reactions in the anode functional layer, should be determined. To determine the contribution of the hydrogen electrochemical reaction in the anode total transfer current density, the charge transfer between the electron and ion conductors is assumed to be the rate determining step of reaction R2, and the effect of the adsorption and dissociation of hydrogen molecules on the electrocatalytic surface of the anode is neglected. The reaction order of unity is also assumed for this reaction in the presence of Ni and YSZ particles. Therefore, the local rate of the forward and backward reactions corresponding to reaction R2, $\vartheta_{f,H_2}(x)$ and $\vartheta_{b,H_2}(x)$, can be expressed as follows

$$\vartheta_{f,H_2}(x) = k_{f,H_2}(x) C_{H_2}(x) \tag{18}$$

$$\vartheta_{b,H_2}(x) = k_{b,H_2}(x) C_{H_2O}(x) \tag{19}$$

where $k_{f,H_2}(x)$ and $k_{b,H_2}(x)$ denote the reaction rate constants for the forward and backward reactions, respectively, and can be estimated from the transition state theory[28]

$$k_{f,H_2}(x) = A_{f,H_2} T_s \exp\left(\frac{-\Delta g_{f,H_2}(x)}{R_u T_s}\right) \tag{20}$$

$$k_{b,H_2}(x) = A_{b,H_2} T_s \exp\left(\frac{-\Delta g_{b,H_2}(x)}{R_u T_s}\right) \tag{21}$$

In these equations, $\Delta g_{f,H_2}(x)$ and $\Delta g_{b,H_2}(x)$ are the actual standard Gibbs function of activation for the forward and backward reactions, respectively. These two parameters can

be expressed in terms of the equilibrium standard Gibbs function of activation and the electron energy change for the anode polarized from the equilibrium state to a desired voltage[29]

$$k_{f,H_2}(x) = A_{f,H_2} T_s \exp\left(\frac{-\Delta g^o_{f,H_2} + 2F\beta(E^o - V(x))}{R_u T_s}\right) \quad (22)$$

$$k_{b,H_2}(x) = A_{b,H_2} T_s \exp\left(\frac{-\Delta g^o_{b,H_2} - 2F(1-\beta)(E^o - V(x))}{R_u T_s}\right) \quad (23)$$

Therefore, the contribution of the hydrogen electrochemical reaction in the anode total transfer current density can be found as follows

$$\begin{aligned} i_{n,H_2}(x) &= 2Fk_{f,H_2}(x)C_{H_2}(x) - 2Fk_{b,H_2}(x)C_{H_2O}(x) \\ &= 2FC_{H_2}(x)A_{f,H_2}T_s \exp\left(\frac{-\Delta g^o_{f,H_2}}{R_u T_s}\right)\exp\left(\frac{2F\beta(E^o_{H_2} - V(x))}{R_u T_s}\right) \\ &\quad - 2FC_{H_2O}(x)A_{b,H_2}T_s \exp\left(\frac{-\Delta g^o_{b,H_2}}{R_u T_s}\right) \\ &\quad \exp\left(\frac{-2F(1-\beta)(E^o_{H_2} - V(x))}{R_u T_s}\right) \end{aligned} \quad (24)$$

At equilibrium, $i_{n,H_2}(x) = 0$, $V(x) = E_{rev,H_2}$, $C_{H_2}(x) = C_{H_2}(0)$, and $C_{H_2O}(x) = C_{H_2O}(0)$. Therefore, the exchange current density corresponding to the hydrogen electrochemical reaction, i_{0,A,H_2}, can be determined from Eq. 24 as follows

$$\begin{aligned} i_{0,A,H_2} &= 2FC_{H_2}(0)A_{f,H_2}T_s \exp\left(\frac{-\Delta g^o_{f,H_2}}{R_u T_s}\right) \\ \exp\left(\frac{2F\beta(E^o_{H_2} - E_{rev,H_2})}{R_u T_s}\right) &= 2FC_{H_2O}(0)A_{b,H_2}T_s \exp\left(\frac{-\Delta g^o_{b,H_2}}{R_u T_s}\right) \\ &\quad \exp\left(\frac{-2F(1-\beta)(E^o_{H_2} - E_{rev,H_2})}{R_u T_s}\right) \end{aligned} \quad (25)$$

And Eq. 24 can be simplified to

$$\begin{aligned} \frac{i_{n,H_2(x)}}{i_{0,A,H_2}} &= \frac{C_{H_2}(x)}{C_{H_2}(0)}\exp\left(\frac{2F\beta(E_{rev,H_2} - V(x))}{R_u T_s}\right) \\ &\quad - \frac{C_{H_2O}(x)}{C_{H_2O}(0)}\exp\left(\frac{-2F(1-\beta)(E_{rev,H_2} - V(x))}{R_u T_s}\right) \end{aligned} \quad (26)$$

If the reversible voltage of the hydrogen electrochemical reaction, E_{rev,H_2}, is obtained from the Nernst relation in Eq. 27 and substituted into Eq. 25, i_{0,A,H_2} can be written as Eq. 28

$$E_{rev,H_2} = E^o_{H_2} + \frac{R_u T_s}{2F}\ln\frac{C_{H_2}(0)}{C_{H_2O}(0)} \quad (27)$$

$$i_{0,A,H_2} = 2FA_{f,H_2}T_s C_{H_2}(0)^{1-\beta} C_{H_2O}(0)^{\beta} \exp\left(\frac{-\Delta g^o_{f,H_2}}{R_u T_s}\right) \quad (28)$$

As the WGS reaction is in equilibrium, the reversible voltage of the hydrogen and carbon monoxide electrochemical reactions are identical, because

$$\begin{aligned} E_{rev,H_2} &= E^o_{H_2} + \frac{R_u T_s}{2F}\ln\frac{C_{H_2}(0)}{C_{H_2O}(0)} = \frac{g^o_{H_2}(T_s) - g^o_{H_2O}(T_s)}{2F} \\ &\quad + \frac{R_u T_s}{2F}\ln\left(K_{p,WGS}(T_s)\frac{C_{CO}(0)}{C_{CO_2}(0)}\right) = \frac{g^o_{H_2}(T_s) - g^o_{H_2O}(T_s)}{2F} \\ &+ \frac{R_u T_s}{2F}\ln\left(\exp\left(-\frac{g^o_{CO_2}(T_s) + g^o_{H_2}(T_s) - g^o_{CO}(T_s) - g^o_{H_2O}(T_s)}{R_u T_s}\right)\right) \\ &+ \frac{R_u T_s}{2F}\ln\left(\frac{C_{CO}(0)}{C_{CO_2}(0)}\right) = \frac{g^o_{CO}(T_s) - g^o_{CO_2}(T_s)}{2F} + \frac{R_u T_s}{2F}\ln\left(\frac{C_{CO}(0)}{C_{CO_2}(0)}\right) \\ &= E^o_{CO} + \frac{R_u T_s}{2F}\ln\left(\frac{C_{CO}(0)}{C_{CO_2}(0)}\right) = E_{rev,Co} \end{aligned} \quad (29)$$

Therefore, the local anode polarization for both hydrogen and carbon monoxide electrochemical reactions are identical

$$\eta_{A,H_2}(x) = E_{rev,H_2} - V(x) = E_{rev,CO} - V(x) = \eta_{A,CO}(x) = \eta_A(x) \quad (30)$$

It was assumed that the gaseous fuel is treated as an ideal gas, $C_i = p_i/(R_u T_s)$. If the transfer coefficient, β, is also assumed to be 0.5,[29] Eqs. 26 and 28 can be expressed as

$$i_{n,H_2}(x) = i_{0,A,H_2}\left[\frac{p_{H_2}(x)}{p_{H_2}(0)}\exp\left(\frac{F\eta_A(x)}{R_u T_s}\right) - \frac{p_{H_2O}(x)}{p_{H_2O}(0)}\exp\left(\frac{-F\eta_A(x)}{R_u T_s}\right)\right] \quad (31)$$

$$i_{0,A,H_2} = \frac{2FA_{f,H_2}}{R_u} p^{0.5}_{H_2}(0) p^{0.5}_{H_2O}(0) \exp\left(\frac{-\Delta g^o_{f,H_2}}{R_u T_s}\right) \quad (32)$$

With the same method and assumptions, the transfer and exchange current densities due to the carbon monoxide electrochemical reaction are found as follows

$$i_{n,CO}(x) = i_{0,A,CO}\left[\frac{p_{CO}(x)}{p_{CO}(0)}\exp\left(\frac{F\eta_A(x)}{R_u T_s}\right) - \frac{p_{CO_2}(x)}{p_{CO_2}(0)}\exp\left(\frac{-F\eta_A(x)}{R_u T_s}\right)\right] \quad (33)$$

$$i_{0,A,CO} = \frac{2FA_{f,CO}}{R_u} p^{0.5}_{CO}(0) p^{0.5}_{CO_2}(0) \exp\left(\frac{-\Delta g^o_{f,CO}}{R_u T_s}\right) \quad (34)$$

After determination of the transfer current densities of hydrogen and carbon monoxide electrochemical reactions, the anode total transfer current density yields as

$$\begin{aligned} i_n(x) &= i_{n,H_2}(x) + i_{n,CO}(x) \\ &= i_{0,A,H_2}\frac{p_{H_2}(x)}{p_{H_2}(0)}\left(1 + \frac{i_{0,A,CO}}{i_{0,A,H_2}} \times \frac{p_{H_2}(0)p_{CO}(x)}{p_{H_2}(x)p_{CO}(0)}\right)\exp\left(\frac{F\eta_A(x)}{R_u T_s}\right) \\ &- i_{0,A,H_2}\frac{p_{H_2O}(x)}{p_{H_2O}(0)}\left(1 + \frac{i_{0,A,CO}}{i_{0,A,H_2}} \times \frac{p_{H_2O}(0)p_{CO_2}(x)}{p_{H_2O}(x)p_{CO_2}(0)}\right)\exp\left(\frac{-F\eta_A(x)}{R_u T_s}\right) \end{aligned} \quad (35)$$

As the WGS reaction is locally in equilibrium

$$K_{p,WGS}(T_s) = \frac{p_{H_2}(0)p_{CO_2}(0)}{p_{H_2O}(0)p_{CO}(0)} = \frac{p_{H_2}(x)p_{CO_2}(x)}{p_{H_2O}(x)p_{CO}(x)}$$
$$or\ \frac{p_{H_2}(0)p_{CO}(x)}{p_{H_2}(x)p_{CO}(0)} = \frac{p_{H_2O}(0)p_{CO_2}(x)}{p_{H_2O}(x)p_{CO_2}(0)} \quad (36)$$

Therefore, Eq. 35 is simplified to

$$i_n(x) = i_{0,A,H_2}\left[\frac{p_{H_2}(x)}{p_{H_2}(0)}\exp\left(\frac{F\eta_A(x)}{R_uT_s}\right) - \frac{p_{H_2O}(x)}{p_{H_2O}(0)}\exp\left(\frac{-F\eta_A(x)}{R_uT_s}\right)\right]\left(1 + \frac{i_{0,A,CO}}{i_{0,A,H_2}} \times \frac{p_{H_2}(0)p_{CO}(x)}{p_{H_2}(x)p_{CO}(0)}\right) \quad (37)$$

It should be noted that the effect of the last parentheses in right hand side of Eq. 37 on the anode local transfer current density is not taken into account if just hydrogen is assumed to be involved in the electrochemical reaction in anode.

For the exchange current densities of hydrogen and carbon monoxide, we developed the following equations from the experimental results of the hydrogen and carbon monoxide electrochemical reactions in the Ni–YSZ anode, reported by Habibzadeh.[30]

$$i_{0,A,H_2} = 86.71p_{H_2}^{0.5}(0)p_{H_2O}^{0.5}(0)\exp\left(\frac{-76,500}{R_uT_s}\right) \quad (38)$$

$$i_{0,A,CO} = 438.7p_{CO}^{0.5}(0)p_{CO_2}^{0.5}(0)\exp\left(\frac{-102,750}{R_uT_s}\right) \quad (39)$$

According to Eq. 37, to determine the anode local transfer current density, we need to determine the anode local polarization and local partial pressures of the fuel species. The following equation is used to determine the anode local polarization[7]

$$\eta_A(x) = E_{rev,H_2} - V(x) = E_{rev,H_2} - (V_{Ni}(x) - V_{YSZ}(x)) \quad (40)$$

Using Ohm's law in Eqs. 41 and 42, the first derivative of $\eta_A(x)$ is expressed as Eq. 43

$$\frac{dV_{Ni}(x)}{dx} = R_{Ni}^{eff}i_{el}(x) \quad (41)$$

$$\frac{dV_{YSZ}(x)}{dx} = R_{YSZ}^{eff}i_{io}(x) \quad (42)$$

$$\frac{d\eta_A(x)}{dx} = -\left(\frac{V_{Ni}(x)}{dx} - \frac{V_{YSZ}(x)}{dx}\right) = R_{YSZ}^{eff}i_{YSZ}(x) - R_{Ni}^{eff}i_{Ni}(x) \quad (43)$$

Using Kirchhoff's circuit law in Eqs. 16 and 17, the second derivative of $\eta_A(x)$ establishes a relation between the anode local polarization and local transfer current density

$$\frac{d^2\eta_A(x)}{dx^2} = R_{YSZ}^{eff}\frac{di_{YSZ}(x)}{dx} - R_{Ni}^{eff}\frac{di_{Ni}(x)}{dx} = (R_{YSZ}^{eff} + R_{Ni}^{eff})A_{TPB}i_n(x), (0.154 < \alpha_{FL} < 6.464) \quad (44)$$

The effective resistivities of Ni and YSZ in Eq. 44 are determined from the random packing sphere method on the basis of the characteristics of the pure materials.[19] The pure electron resistivity of Ni and ion resistivity of YSZ are estimated from Eqs. 45[10] and 46,[19] respectively.

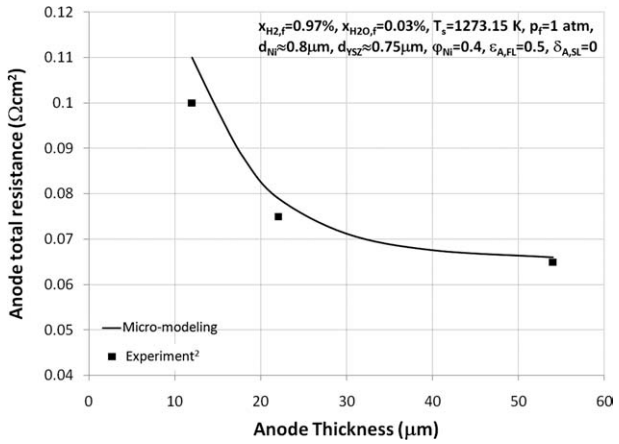

Figure 3. The results obtained from the modeling and experiment for the anode samples fabricated by Brown et al.[2]

$$R_{Ni}^0 = (3.27 \times 10^6 - 1065.3T_s)^{-1} \quad (45)$$

$$R_{YSZ}^0 = 1.263 \times 10^{-9}T_s\exp\left(\frac{111000}{R_uT_s}\right) \quad (46)$$

The local partial pressure of the fuel components in the functional layer is determined with the similar model and assumptions considered for the substrate layer. The only difference is the effect of the hydrogen and carbon monoxide consumptions through electrochemical reactions that should be taken into account in the mass conservation equation (see Figure 2). From the mass conservation equation, the rate of flux of hydrogen and carbon monoxide in x direction are determined as Eqs. 47 and 48 that should be substituted instead of Eqs. 10 and 11, respectively.

$$\frac{d\dot{n}_{H_2}''(x)}{dx} = -\dot{C}_{H_2}'''(x) + \dot{C}_{H_2O,WGS}'''(x) \quad (47)$$

$$\frac{d\dot{n}_{CO}''(x)}{dx} = -\dot{C}_{CO}'''(x) - \dot{C}_{H_2O,WGS}'''(x) \quad (48)$$

where the rate of hydrogen and carbon monoxide consumptions, $\dot{C}_{H_2}'''(x)$ and $\dot{C}_{CO}'''(x)$, respectively, are dependent on the transfer current density corresponding to the hydrogen and carbon monoxide electrochemical reactions

$$\dot{C}_{H_2}'''(x) = \frac{A_{TPB}}{2F}i_{n,H_2(x)} \quad (49)$$

$$\dot{C}_{CO}'''(x) = \frac{A_{TPB}}{2F}i_{n,CO}(x) \quad (50)$$

Therefore, the anode local transfer current density, local polarization, and local partial pressures of the fuel species are coupled and the system of Eqs. 51 should be solved with the associated boundary conditions to determine the distribution of these variables along the anode functional layer.

$$
\begin{cases}
\dfrac{d^2\eta_{\mathrm{A}}(x)}{dx^2} = (R_{\mathrm{YSZ}}^{\mathrm{eff}} + R_{\mathrm{Ni}}^{\mathrm{eff}}) A_{\mathrm{TPB}} i_n(x) \\
i_n(x) = i_{0,\mathrm{A},\mathrm{H_2}} \\
\quad \times \left[\dfrac{p_{\mathrm{H_2}}(x)}{p_{\mathrm{H_2}}(0)} \exp\left(\dfrac{F\eta_{\mathrm{A}}(x)}{R_{\mathrm{u}} T_{\mathrm{s}}} \right) - \dfrac{p_{\mathrm{H_2O}}(x)}{p_{\mathrm{H_2O}}(0)} \exp\left(\dfrac{-F\eta_{\mathrm{A}}(x)}{R_{\mathrm{u}} T_{\mathrm{s}}} \right) \right] \\
\quad \times \left(1 + \dfrac{i_{0,\mathrm{A},\mathrm{CO}}}{i_{0,\mathrm{A},\mathrm{H_2}}} \times \dfrac{p_{\mathrm{H_2}}(0) p_{\mathrm{CO}}(x)}{p_{\mathrm{H_2}}(x) p_{\mathrm{CO}}(0)} \right) \\
\dfrac{dp_l(x)}{dx} = -\dfrac{R_{\mathrm{u}} T_{\mathrm{s}}}{\sum_{m=1}^{n} p_m(x)} \sum_{m=1}^{n} \dfrac{p_m(x)\dot{n}_l''(x) - p_l(x)\dot{n}_m''(x)}{D_{l-m}^{\mathrm{eff}}} \\
\quad - R_{\mathrm{u}} T_{\mathrm{s}} \dfrac{\dot{n}_l''(x)}{D_{\mathrm{K},l}^{\mathrm{eff}}} + R_{\mathrm{u}} T_{\mathrm{s}} \dfrac{\beta_0 p_l(x)}{D_{\mathrm{K},l}^{\mathrm{eff}} \mu(x)} \times \dfrac{\sum_{m=1}^{n} \frac{\dot{n}_m''(x)}{D_{\mathrm{K},m}^{\mathrm{eff}}}}{\left(1 + \frac{\beta_0}{\mu(x)} \sum_{m=1}^{n} \frac{p_m(x)}{D_{\mathrm{K},m}^{\mathrm{eff}}} \right)} \\
\quad l \in \{\mathrm{H_2}, \mathrm{CO}, \mathrm{H_2O}, \mathrm{CO_2}, \mathrm{CH_4}, \mathrm{N_2}\} \\
\dfrac{d\dot{n}_{\mathrm{H_2}}''(x)}{dx} = -\dfrac{A_{\mathrm{TPB}}}{2F} i_{0,\mathrm{A},\mathrm{H_2}} \\
\quad \times \left[\dfrac{p_{\mathrm{H_2}}(x)}{p_{\mathrm{H_2}}(0)} \exp\left(\dfrac{F\eta_{\mathrm{A}}(x)}{R_{\mathrm{u}} T_{\mathrm{s}}} \right) - \dfrac{p_{\mathrm{H_2O}}(x)}{p_{\mathrm{H_2O}}(0)} \exp\left(\dfrac{-F\eta_{\mathrm{A}}(x)}{R_{\mathrm{u}} T_{\mathrm{s}}} \right) \right] \\
\quad + \dot{C}_{\mathrm{H_2O,WGS}}'''(x) \\
\dfrac{d\dot{n}_{\mathrm{CO}}''(x)}{dx} = -\dfrac{A_{\mathrm{TPB}}}{2F} i_{0,\mathrm{A},\mathrm{CO}} \\
\quad \times \left[\dfrac{p_{\mathrm{CO}}(x)}{p_{CO}(0)} \exp\left(\dfrac{F\eta_{\mathrm{A}}(x)}{R_{\mathrm{u}} T_{\mathrm{s}}} \right) - \dfrac{p_{\mathrm{CO_2}}(x)}{p_{\mathrm{CO_2}}(0)} \exp\left(\dfrac{-F\eta_{\mathrm{A}}(x)}{R_{\mathrm{u}} T_{\mathrm{s}}} \right) \right] \\
\quad - \dot{C}_{\mathrm{H_2O,WGS}}'''(x) \\
\dot{n}_{\mathrm{H_2O}}''(x) = -\dot{n}_{\mathrm{H_2}}''(x) \\
\dot{n}_{\mathrm{CO_2}}''(x) = -\dot{n}_{\mathrm{CO}}''(x) \\
\dot{n}_{\mathrm{CH_4}}''(x) = -\dot{n}_{\mathrm{N_2}}''(x) = 0 \\
K_{\mathrm{p,WGS}}(T_s) = \dfrac{p_{\mathrm{H_2}}(x) p_{\mathrm{CO_2}}(x)}{p_{\mathrm{H_2O}}(x) p_{\mathrm{CO}}(x)}
\end{cases}
\tag{51}
$$

$$
\mathrm{AT}\ x = \delta_{\mathrm{A,SL}} : d\eta_A/dx = -R_{Ni}^{eff} i_{tot}; p_l = p_l(\delta_{SL}),
$$
$$
l \in \{H_2, CO, H_2O, CO_2, CH_4, N_2\}
$$

$$
\mathrm{AT}\ x = \delta_{\mathrm{A}} : d\eta_A/dx = R_{YSZ}^{eff} i_{tot}, \dot{n}_{H_2}'' = 0, \dot{n}_{CO}'' = 0
$$

After solving the system of Eqs. 51, the distribution of current densities corresponding to the hydrogen and carbon monoxide electrochemical reactions can be determined from the following differential equations

$$
di_{\mathrm{Ni,H_2}}(x) = -A_{\mathrm{TPB}} i_{n,\mathrm{H_2}}(x) \tag{52}
$$

$$
di_{\mathrm{Ni,CO}}(x) = -A_{\mathrm{TPB}} i_{n,\mathrm{CO}}(x) \tag{53}
$$

Finally, the total polarization and total resistance of anode are determined from Eqs. 54 and 55, respectively.[31] As the ohmic polarization in the substrate layer is negligible, we did not consider the effect of this polarization in Eq. 54.

$$
\eta_{\mathrm{A,tot}} = \frac{R_{\mathrm{Ni}}^{\mathrm{eff}} R_{\mathrm{YSZ}}^{\mathrm{eff}}}{R_{\mathrm{Ni}}^{\mathrm{eff}} + R_{\mathrm{YSZ}}^{\mathrm{eff}}} \left(\frac{\eta_A(\delta_{\mathrm{A,SL}})}{R_{\mathrm{YSZ}}^{\mathrm{eff}}} + i_{\mathrm{tot}} \delta_{A,FL} + \frac{\eta_A(\delta_A)}{R_{\mathrm{Ni}}^{\mathrm{eff}}} \right) \tag{54}
$$

$$
R_{\mathrm{A,tot}} = \frac{\eta_{\mathrm{A,tot}}}{i_{\mathrm{tot}}} \tag{55}
$$

Validation of the Model

We developed a computer code on the basis of the anode micromodel and simulated the porous Ni–YSZ anode samples fabricated by Brown et al.[2] and Matsuzaki and Yasuda[1] Brown et al.[2] have conducted several experiments on hydrogen-fuelled Ni–YSZ anode samples ($d_{\mathrm{Ni}} \approx 0.8$ μm, $d_{\mathrm{YSZ}} \approx 0.75$ μm, $\varphi_{\mathrm{Ni}} \approx 0.4$, and $\varepsilon_{\mathrm{A,FL}}$=0.5) to correlate the anode total resistance to the anode thickness at pressure of 1 atm and temperature of 1273.15 K. As seen in Figure 3, despite the limited experimental points available, the micromodel shows reasonability good agreement with experiment for hydrogen fuel with the average relative error of $\sim$ 5.6%.

Matsuzaki and Yasuda[1] have also conducted several experiments on a anode sample ($d_{\mathrm{Ni}} = 0.9$ μm, $\varphi_{\mathrm{Ni}} \approx 0.8$, $\delta_{\mathrm{A,FL}} = 25$ μm, and $\varepsilon_{\mathrm{A,FL}} = 0.45$) to correlate the anode total polarization to the current density at pressure of 1 atm and temperature of 1023.15 K for the fuel group 1 (fuel Nos. 1–3) and temperature of 1273.15 K for the fuel group 2 (fuel Nos. 4–6) in Table 1. They did not report the size of the YSZ particles; however, if this size is assumed to be 0.15 μm, the anode total polarization obtained from the computer code and reported for one of the experimental points for hydrogen fuel ($x_{H_2} = 78.5\%$, $x_{H_2O} = 21.5\%$, $T_{\mathrm{s}} = 1273.15$ K, and $i_{\mathrm{tot}} = 0.3$ A/m^2) are almost identical. We assumed this value for the size of YSZ particles and investigated the validity of the micromodel for the other experimental points for different fuels listed in Table 1.

As seen in Figure 4, the effect of the composition of fuels on the change of anode total polarization predicted by the computer simulation is in good agreement with experiments reported by Matsuzaki and Yasuda.[1] The value of the anode total polarization at different current densities and temperatures can be also predicted with the average relative error of $\sim$8.8%.

Table 1. The Composition of the Fuels in the Experiments Conducted by Matsuzaki et al.[1]

Fuel							
Group	No.	H_2 (%)	CO (%)	H_2O (%)	CO_2 (%)	$\log(p_{O_2})_{\mathrm{anode}}$ (atm)	Temp. (K)
1	1	64.2	14.9	16.0	4.9	−20.75	1023.15
	2	38.8	38.8	9.7	12.6	−20.75	1023.15
	3	18.8	57.8	4.7	18.8	−20.75	1023.15
2	4	62.8	17.2	17.2	2.8	−15.69	1273.15
	5	41.0	41.0	11.2	6.8	−15.69	1273.15
	6	12.0	72.8	3.3	12.0	−15.69	1273.15

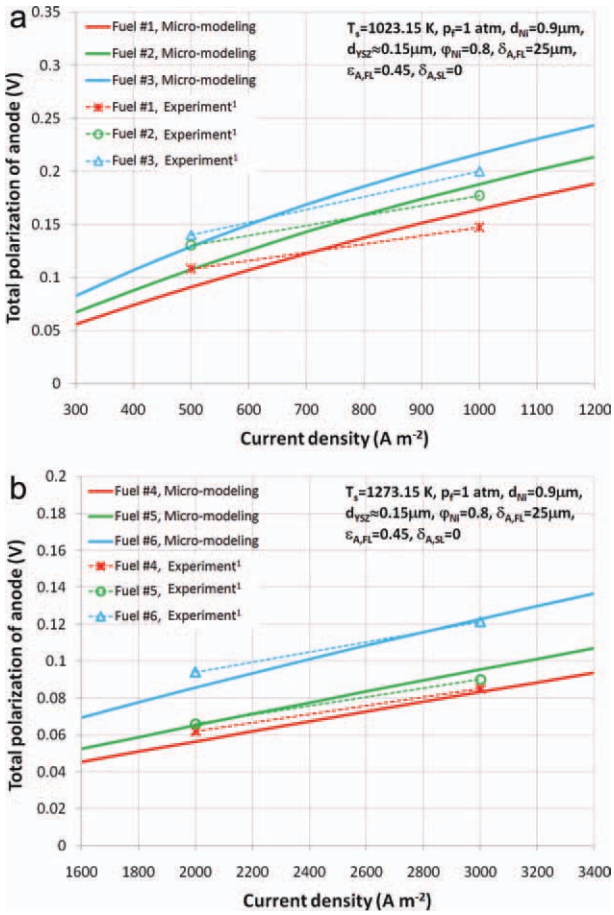

Figure 4. The results obtained from the micromodel and experiment for the anode sample tested by Matsuzaki et al.[1]: (a) T_s = 1023.15 and (b) T_s = 1273.15 K.

[Color figure can be viewed in the online issue, which is available at wileyonlinelibrary.com.]

Results

Although various fuels containing CH_4, H_2, CO, H_2O, CO_2, and N_2 can be considered as the input data for the anode micromodel developed, the average composition of the biogas produced in wastewater treatment plants in Ontario is selected as the fuel in this study. This biogas contains methane (62.0%), carbon dioxide (35.5%), nitrogen (2.45%), and water vapor (0.01%).[32,33] As explained in Refs. [34] and [35], due to the carbon deposition issue over the anode catalyst, the biogas cannot be fed directly to the anode; however, it can be processed using several methods, such as the anode exit gas recirculation (AGR), external steam reformer (SR), external partial oxidation (POX),[36,37] or even carbon decomposition methods.[38,39] The compositions of the biogas processed by AGR, SR, and POX methods at temperature of 1073.15 K and pressure of 1 atm are listed in Table 2. These compositions are used as the boundary conditions of the system of Eqs. 15 at $x = 0$. As the air is used as the reforming agent for POX method, the nitrogen content of the fuel processed by this method is significantly higher than that processed by AGR or SR methods.

Table 2. Compositions of the Biogas Processed by AGR, SR, and POX Methods at Temperature of 1073.15 K and Pressure of 1 atm

	Biogas processing method		
Composition (%)	Anode gas recirculation	Steam reforming	Partial oxidation
CH_4	1.2	1.5	0.77
H_2	51.5	57.4	40.6
CO	40.9	35.6	32.2
H_2O	2.8	2.7	1.7
CO_2	2.4	1.8	1.5
N_2	1.2	1.0	23.2

The porous composite anode considered in this study is fabricated with Ni particles, as the electron conductor, and YSZ particles with the chemical composition of $(ZrO_2)_{0.92}(Y_2O_3)_{0.08}$, as the ion conductor. This anode operates at the current density of 5000 A/m^2, temperature of 1073.15 K, and fuel pressure of 1 atm. The microstructure of this anode consists of two layers of the substrate layer with the thickness of 472.5 mm, porosity of 0.4, and particles size of 2.5 mm, and the functional layer with the Ni particle size of 1 mm, Ni volume ratio of 0.428, particle-size ratio of unity, thickness of 45 mm, and porosity of 0.33.

Distribution of the mole fraction of H_2, CO, H_2O, and CO_2

As shown in Figure 5, the mole fraction of H_2 and CO decreases linearly with a slight slop along the substrate layer and changes approximately as a concave upward parabolic curve, with a minimum located at the interface of the anode and electrolyte, along the functional layer for the biogas processed by AGR, SR, and POX methods. The results indicate that the mole fraction of H_2 and CO in the bulk fuel stream decreases 2.4% and 5.4%, respectively, for the biogas processed by AGR or SR method, and 2.9% and 6.6%, respectively, for the biogas processed by POX method, at

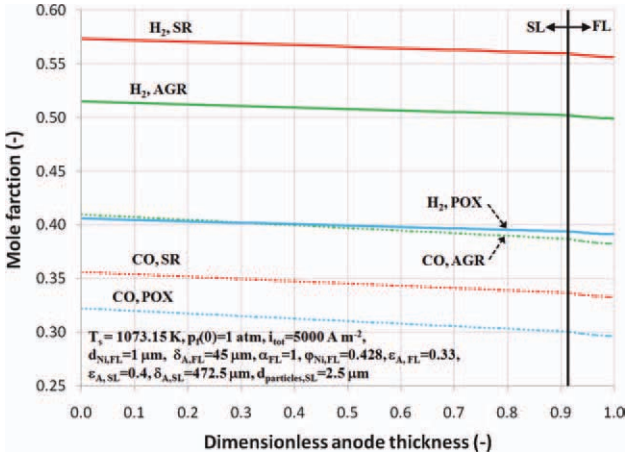

Figure 5. Distribution of the mole fraction of H_2 and CO along the thickness of the anode substrate (SL) and functional (FL) layers.

[Color figure can be viewed in the online issue, which is available at wileyonlinelibrary.com.]

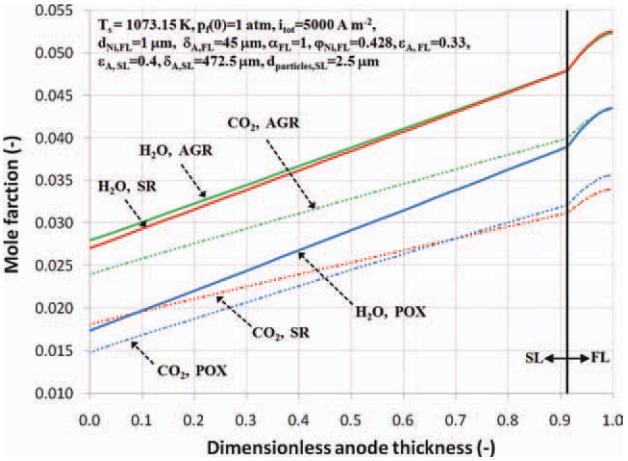

Figure 6. Distribution of the mole fraction of H_2O and CO_2 along the thickness of the anode substrate (SL) and functional (FL) layers.

[Color figure can be viewed in the online issue, which is available at wileyonlinelibrary.com.]

the interface of the substrate and functional layers. From this interface to the interface of the anode and electrolyte, the mole fraction of H_2 and CO decreases an additional 0.6% and 1.2%, respectively, for the biogas processed by AGR or SR method, and 0.7% and 1.4%, respectively, for the biogas processed by POX method.

In contrast to the H_2 and CO, the mole fraction of H_2O and CO_2 changes significantly in both the substrate and the functional layers (see Figure 6); as such their value in the bulk fuel stream increases linearly 70%, 76%, and 122% for H_2O and 66%, 71%, and 115% for CO_2 for the biogas processed by AGR, SR, and POX methods, respectively, at the interface of the substrate and functional layers. In the functional layer, the mole fraction of H_2O and CO_2 increases as a convex upward parabolic curve with a maximum value located at the interface of the anode and electrolyte. From the interface of the substrate and functional layers to the interface of the anode and electrolyte, an additional 9%, 10%, and 12% for H_2O and 8%, 9%, and 11% for CO_2, for the biogas processed by AGR, SR, and POX methods, respectively, is predicted.

As a general result, the change of the mole fraction of the fuel species for the biogas processed by POX method is greater than that for the biogas processed by AGR or SR method. It may be due to the presence of the high amount of nitrogen in the fuel processed by POX method. Therefore, it is expected that the limiting current density of the anode fuelled by the biogas processed by POX method is less than that of the anode fuelled by the biogas processed by AGR or SR method.

Distribution of the rate of consumption of H_2, CO, and H_2O

The rate of consumption of H_2 and CO due to the electrochemical reactions R2 and R3, and H_2O due to the WGS reaction R1 along the functional layer is shown in Figure 7. As seen in this figure, the rate of these reactions increases as a concave upward parabolic curve along the functional layer and the maximum rate achieves at the interface of the anode and electrolyte. The results also indicate that the rate of these reactions is approximately identical for the biogas processed by AGR and POX methods. In contrast to the consumption rate of CO and H_2O, the local consumption rate of H_2 for the biogas processed by SR method is higher than that for the biogas processed by AGR or POX method. As a remarkable result, the ratio of the consumption rate of H_2 and CO due to the electrochemical reactions is $\sim$ 6.0 for the biogas processed by SR method, and 4.7 for the biogas processed by AGR or POX method. Moreover, the consumption rate of CO due to the electrochemical reaction R3 is slightly higher than the consumption rate of H_2O due to the WGS reaction R1 for the biogas processed by AGR or POX method. These consumption rates are approximately identical for the biogas processed by SR method. It means that the amount of CO contributed indirectly in the H_2 electrochemical reaction, after converting to H_2 through WGS reaction, is almost identical to the CO consumed directly through CO electrochemical reaction.

Our studies in the anode substrate layer revealed that H_2O is slightly consumed through the WGS reaction along the substrate layer. This is due to the fact that the WGS reaction should be locally kept in equilibrium at the operating temperature of 1073.15 K. In addition, no electrooxidation reaction occurs in the substrate layer. Hence, the x-axis in Figure 7 covers only the dimensionless thickness of the functional layer.

Distribution of the rate of flux of H_2 and CO

As shown in Figure 8, the rate of flux of H_2 increases and CO decreases linearly with a slight slope along the substrate layer due to the conversion of CO to H_2 through WGS reaction R1; then, the rate of flux of H_2 and CO decreases sharply along the functional layer and approaches zero at the interface of the anode and electrolyte due to the consumption of H_2 and CO through the electrochemical reactions. It is noted that the rate of flux of H_2O and CO_2 in anode is equal

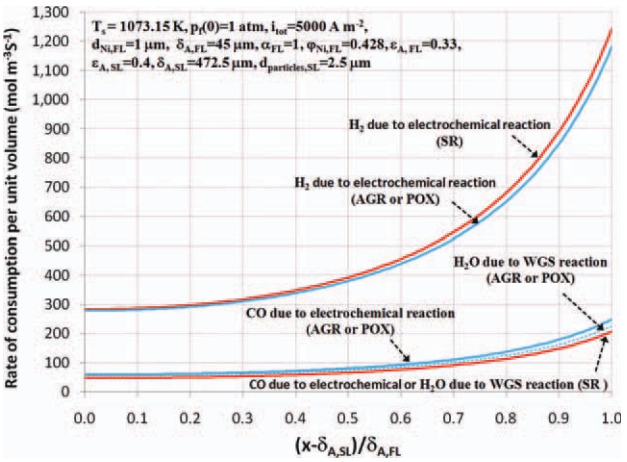

Figure 7. Distribution of the rate of consumption of H_2, CO, and H_2O along the thickness of the anode functional layer.

[Color figure can be viewed in the online issue, which is available at wileyonlinelibrary.com.]

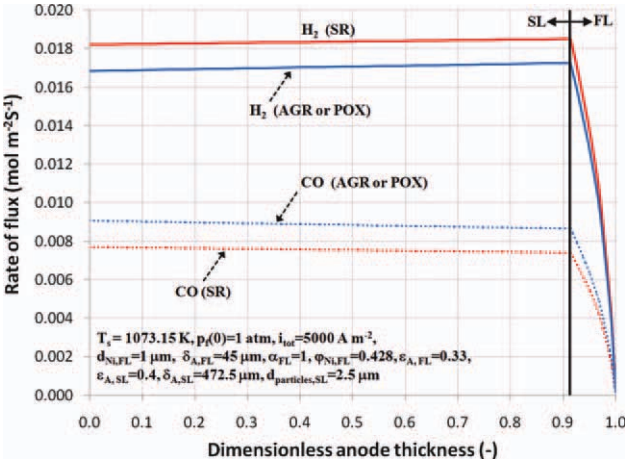

Figure 8. Distribution of the rate of flux of H_2 and CO along the thickness of the anode substrate (SL) and functional (FL) layers.

[Color figure can be viewed in the online issue, which is available at wileyonlinelibrary.com.]

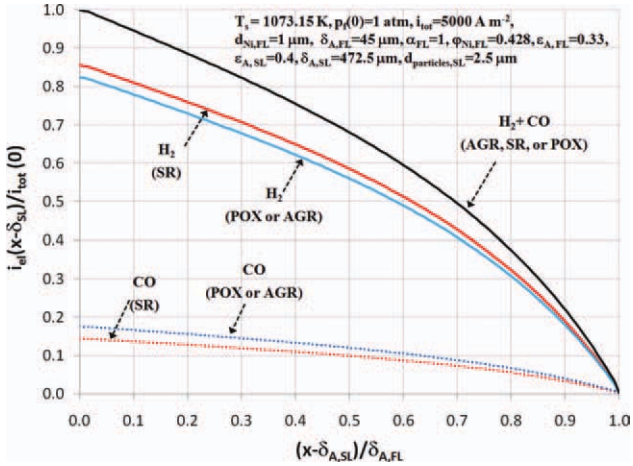

Figure 9. Distribution of the current density along the thickness of the anode functional layer.

[Color figure can be viewed in the online issue, which is available at wileyonlinelibrary.com.]

in magnitude and opposite in direction compared with that of H_2 and CO, respectively, in entire the anode thickness. The results also indicate that the rate of flux of H_2 and CO for the biogas processed by AGR and POX methods are identical. As a remarkable result, the ratio of the rate of flux of H_2 and CO at the entrance of the anode is approximately 2.4 and 1.9 for the biogas processed by SR and AGR/POX methods, respectively.

Distribution of the current density

The distribution of the current density generated through H_2 and CO electrochemical reactions along the thickness of the functional layer is shown in Figure 9. The distribution of the total current generated (H_2 + CO) is independent of the method used to process biogas. The results indicate that 50% of the total current is generated within 30% of the functional layer near the anode and electrolyte interface. It means, 50% of the electrochemical reactions R2 and R3 take place within 30% of the functional layer near the anode and electrolyte interface. This is due to the significantly higher the ionic resistivity of YSZ than the electronic resistivity of Ni that leads to the rate of electrochemical reactions is higher, where the length of the ion transport is shorter. The results also indicate that only 11% of the electric current is generated within 20% of the functional layer near the functional and substrate layers.

Distribution of the polarization

As shown in Figure 10, the local anode polarization increases along the thickness of the functional layer, approximately as a concave upward parabolic curve. The increase of the local polarization is negligible at the interface of the substrate and functional layers, and reaches the maximum at the anode and electrolyte interface. This is due to that fact that the maximum electric current is generated at the interface of the anode and electrolyte, where the transport length of ionic charges approaches zero. As a remarkable result, the local polarization for the biogas processed by AGR and SR methods is approximately identical in the entire functional layer, and less than that for the biogas processed by POX methods.

Effect of the microstructural variables on the anode total resistance

We reported in our another article that for a given operating condition, the electrochemical performance of porous composite electrodes is dependent on the microstructural variables of the porosity, thickness, particle-size ratio, and particle size and volume fraction of the electron conducting particles.[19] As the porous composite anode studied in this article is made of the substrate and functional layers, the microstructural variables of these two layers affect the anode electrochemical performance.

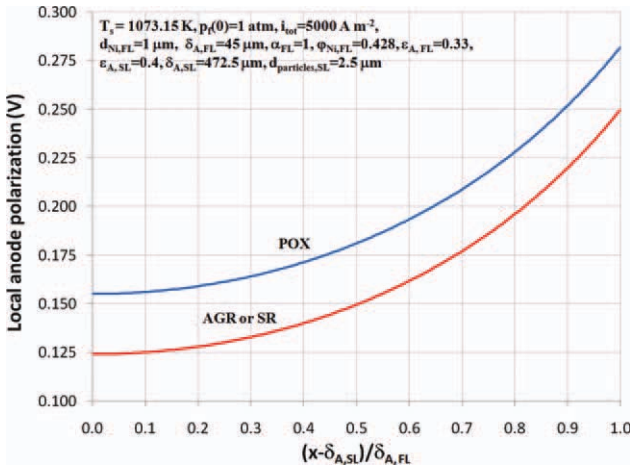

Figure 10. Distribution of the polarization along the thickness of the anode functional layer.

[Color figure can be viewed in the online issue, which is available at wileyonlinelibrary.com.]

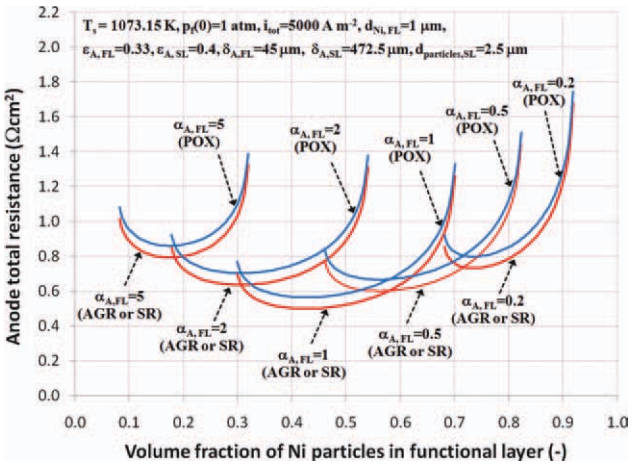

Figure 11. Effect of the Ni volume fraction of the functional layer at different particle-size ratios on the anode total resistance.

[Color figure can be viewed in the online issue, which is available at wileyonlinelibrary.com.]

No electrochemical reactions occur in the substrate layer; hence, the volume fraction of Ni particles is not limited to the percolation threshold of the YSZ particles and can be increased to unity to minimize the ohmic polarization. Of course, the contribution of this polarization in the total anode polarization is negligible, if the Ni volume fraction is fairly beyond its corresponding percolation threshold. Therefore, the Ni volume fraction in the substrate layer may be selected on the basis of matching the thermal expansion coefficient of the functional and substrate layers and/or controlling the rate of the steam reforming reaction at the interface of the bulk fuel flow and substrate layer rather than the electrochemical performance studies. In this study, it is assumed that the volume fraction of Ni particles in the substrate layer is beyond its corresponding percolation threshold, so as the ohmic polarization in this layer is negligible. If it is assumed that the size of the YSZ and Ni particles are equal in this layer, the anode electrochemical performance will be dependent on the microstructural variables of the porosity, thickness, and particle size of the anode substrate layer, and the porosity, thickness, particle-size ratio, and particle size and volume fraction of Ni particles of the anode functional layer.

The effect of the Ni volume fraction of the functional layer on the anode total resistance is shown in Figure 11. As seen, with an increase in the volume fraction of Ni particles, the anode total resistance decreases to a certain value and then increases. Therefore, there is an optimum Ni volume fraction at which the anode total resistance is minimized. Our studies confirm that there is always such an optimum Ni volume fraction that minimizes the anode total resistance. For the particle-size ratios greater than unity, this optimum volume fraction is not expected to be among the Ni volume fractions in the range of $(3.38\alpha_{A,FL} + 2.4)/(2.4\alpha_{A,FL}^2+6.76\alpha_{A,FL}+2.4)$ and $1/(\alpha_{A,FL}/2.4 + 1)$, because with an increase in the Ni volume fraction in this range, the electrochemical active area and pore size decrease and the effective resistivity of YSZ increases and consequently, all three activation, concentration, and ohmic polarizations in the functional layer increases.[19] This would be valid for the particle-size ratios less than unity, if the pore size is not too small to inhibit the fuel species transport from the bulk to the active sites of the anode.

The effect of the particle-size ratio is also shown in Figure 11. As seen in this figure, among the optimum Ni volume fractions obtained at different particle-size ratios, the one obtained at the particle-size ratio of unity provides the lowest total resistance. Our studies confirm that this result can be generalized for any anode microstructural variables and operating conditions of SOFCs. Indeed, for an anode microstructure with the optimum Ni volume fraction, the optimum particle-size ratio is equal to 1.

The effect of the Ni particle size of the functional and substrate layers on the anode total resistance for the anode functional layer with the optimum Ni volume fraction (=0.428), and particle-size ratio of unity is shown in Figure 12. With a decrease in the Ni particle size of the functional layer, the anode total resistance decreases to a certain value and then increases. Therefore, there is an optimum size for the Ni particles at which the anode total resistance is minimized. It is noted that for the particle-size ratio of unity, with a decrease in the Ni particle size, the activation polarization decreases due to the increase in the electrochemical active area, the concentration polarization increases due to the decrease in the average pore size, and the ohmic polarization remain constant, because the effective resistivities of the Ni and YSZ are not a function of the size of particles.[19] As the contribution of the activation polarization in the anode total resistance is greater than that of the concentration polarization for the Ni particles larger than the optimum size, the anode total resistance decreases with a decrease in the Ni particle size. In contrast, for the Ni particles smaller than the optimum size, the contribution of the concentration polarization is greater than that of the activation polarization;

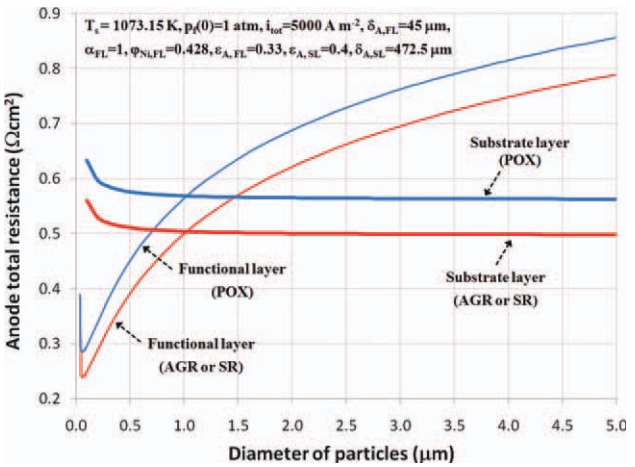

Figure 12. Effect of the Ni particle size in the anode functional ($d_{particles,SL}$ = 2.5 μm) and substrate ($d_{Ni,FL}$ = 1 μm) layers on the anode total resistance.

[Color figure can be viewed in the online issue, which is available at wileyonlinelibrary.com.]

hence, the anode total resistance increases with a decrease in the size of the Ni particles.

As shown in Figure 12, the optimum size of the Ni particles is smaller than 0.1 μm for the anode studied. Although using the Ni particles in the range of the optimum size leads to a decrease in the anode total resistance, the anode may be vulnerable to degradation due to an extensive grain growth of the particles during the sintering process or operation.[40,41] The grain growth reduces significantly the active area and leads to an increase in the total resistance. This necessitates the optimum Ni particle size to be selected by durability analysis rather than the electrochemical performance analysis in this article.

The increase in the size of the particles in the substrate layer leads to a decrease in the anode total resistance due to the decrease in the concentration polarization in the substrate layer; however, the total resistance does not change considerably for the particle sizes greater than 1.5 μm.

The effect of the thickness of the anode functional and substrate layers on the anode total resistance, for the anode functional layer with the Ni volume fraction of 0.428 and particle-size ratio of unity, is shown in Figure 13. As seen, with an increase in the thickness of the functional layer, the anode total resistance decreases to a certain value and then increases linearly with a slight slope. Hence, there is an optimum value for the thickness of the functional layer at which the total resistance is minimized. This trend makes sense physically, because for thin anode functional layers (e.g., $<$10 μm) the activation polarization increases significantly due to the insufficient active sites for the H_2 and CO electrochemical reactions. For thick functional layers (e.g., $>$100 μm), the contribution of ohmic and concentration polarizations become significant because of the increase in the mass and charge transport length. For the anode studied in this article, the optimum thickness of the functional layer is predicted to be approximately 95 and 102 μm for the biogas processed by AGR/SR and POX methods, respectively.

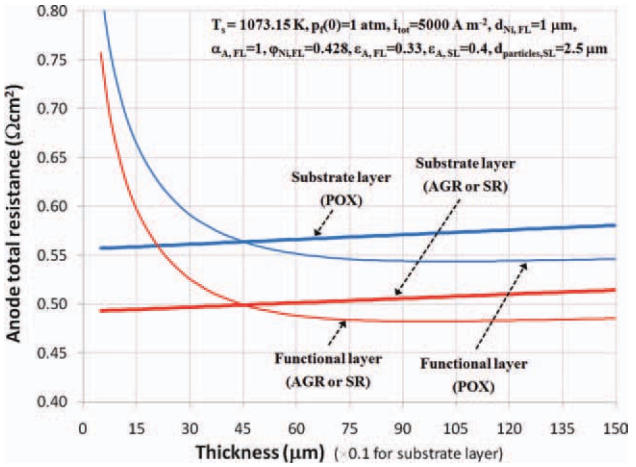

Figure 13. Effect of the thickness of the anode functional ($\delta_{A,SL}$ = 472.5 μm) and substrate ($\delta_{A,FL}$ = 45 μm) layers on the anode total resistance.

[Color figure can be viewed in the online issue, which is available at wileyonlinelibrary.com.]

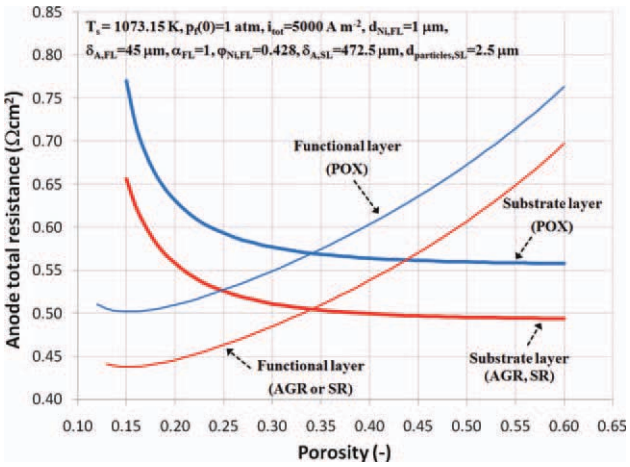

Figure 14. Effect of the porosity of the anode functional ($\varepsilon_{A,SL}$ = 0.4) and substrate ($\varepsilon_{A,FL}$ = 0.33) layers on the anode total resistance.

[Color figure can be viewed in the online issue, which is available at wileyonlinelibrary.com.]

The anode total polarization is also increased linearly with a slight slope with an increase in the thickness of the substrate layer because of the increase in the mass transport length of fuel that leads to an increase in the anode concentration polarization; therefore, the minimum thickness required for the mechanical strength of the cell should be selected for the substrate layer.

The effect of the porosity of the anode functional and substrate layers on the anode total resistance, for the anode functional layer with the Ni volume fraction of 0.428 and particle-size ratio of unity, is shown in Figure 14. With a decrease in the porosity of the functional layer, the anode total resistance decreases to a certain value due to the decrease in the activation and ohmic polarizations and then increases suddenly due to a significant increase in the concentration polarization. Therefore, there is a porosity at which the anode total resistance is minimized. For the anode studied in this article, the optimum porosity of the functional layer is obtained 0.15 for the biogas processed by AGR, SR, or POX method. For a random packing of spherical particles with a given size, the porosity may not be less than a certain value, if the average contact angle between particles is not increased during the sintering process. In such a situation, if the porosity of 0.15 is not achievable, the minimum possible porosity for the functional layer should be considered.

In the substrate layer, for the porosity of less than 0.25, the decrease in the porosity leads to a significant increase in the anode total resistance because of the significant increase in the concentration polarization. However, for the porosity of greater than 0.45 the anode total resistance is a weak function of the porosity.

Conclusions

A comprehensive anode micromodel to predict the electrochemical performance of the hydrocarbon-fuelled porous composite anodes with various microstructural variables was developed, and its validity for several fuels and different

temperatures and current densities was verified. As a case study, a biogas-fuelled porous Ni–YSZ anode with substrate and functional layers was simulated. The results of the simulation indicated that the change of the mole fraction of fuel species along the anode thickness for the biogas processed by POX method is more than that for the biogas processed by AGR or SR methods. The ratio of the rate of consumption of H_2 and CO due to the electrochemical reactions is ~6.0 for the biogas processed by SR method and 4.7 for the biogas processed by AGR/POX method. However, the ratio of the rate of flux of H_2 and CO at the entrance of the anode is approximately 2.4 and 1.9 for the biogas processed by SR and AGR/POX methods, respectively. The results also revealed that 50% of the total current is generated within 30% of the functional layer near the anode and electrolyte interface and only 11% of the electric current is generated within 20% of the functional layer near the functional and substrate layers.

The results of this study for the microstructure of the functional layer confirmed that there is always an optimum Ni volume fraction at which the anode total resistance is minimized. Among the optimum Ni volume fractions obtained at different particle-size ratios, the one obtained at the particle-size ratio of unity always provides the lowest total resistance. For any microstructure of the functional layer with the optimum Ni volume fraction and particle-size ratio of unity, there is an optimum Ni particle size, thickness and porosity at which the anode total resistance is minimized. For the microstructure of the substrate layer, the anode total resistance increases significantly if the size of the particles and porosity are less than 1.5 μm and 0.3, respectively. Therefore, to decrease the anode total polarization resistance, a special consideration to select/control the microstructure of porous composite anodes for both substrate and functional layers before/during the fabrication process is required.

Acknowledgments

The authors gratefully acknowledge the financial support provided by Natural Sciences and Engineering Research Council (NSERC) of Canada.

Notation

A_{TPB} = electrochemical active area per unit volume, m^2/m^3
A = coefficient of reaction rate constant, m/(s K)
C_m = concentration, mol/m^3
$\dot{C}$ = rate of consumption, $mol/(m^3\ s)$
d = diameter, m
D = diffusivity, m^2/s
E° = standard voltage, V
E_{rev} = reversible voltage, V
F = Faraday's constant, C/mol
g = molar Gibbs free energy, J/mol
i = current density, A/m^2
i_0 = exchange current density, A/m^2
i_n = transfer current density per unit of electrochemical active area, A/m^2
k = reaction rate constant, m/s
K_p = equilibrium constant at constant pressure
MW = molecular weight, kg/kmol
$\dot{n}''$ = rate of flux, $mol/(m^2\ s)$
p = pressure, Pa
R = resistivity, Ω m
$R_{A,tot}$ = anode total resistance, $\Omega\ m^2$
R_u = universal gas constant, J/(mol K)
T = temperature, K
V = voltage, V
x = spatial coordinate along the anode thickness

Greek letters

α = particle-size ratio, d_{YSZ}/d_{Ni}
β = transfer coefficient
β_0 = flow permeability, m^2
δ = Thickness, m
ε = porosity
η = Polarization, V
ϑ = rate of reaction, $mol/(m^2\ s)$
μ = dynamic viscosity, kg/(m s)
φ = volume fraction of electron or ion conducting particle
θ_c = contact angle between the electron and ion conducting particle, rad
τ = tortuosity

Subscripts

A = anode
b = backward reaction
C = cathode
E = electrolyte
el = electron conducting particle
f = forward reaction
F = fuel
FL = functional layer
io = ion conducting particle
K = Knudsen diffusion
l = l^{th} component of the fuel
m = m^{th} component of the fuel
n = number of components of the fuel
s = solid structure of the anode
SL = substrate layer
tot = total
WGS = water gas shift reaction

Superscripts

0 = pure material
eff = effective
o = standard pressure

Literature Cited

1. Matsuzaki Y, Yasuda I. Electrochemical oxidation of H_2 and CO in a H_2–H_2O–CO–CO_2 system at the interface of a Ni–YSZ cermet electrode and YSZ electrolyte. *J Electrochem Soc*. 2000;147:1630–1635.
2. Brown M, Primdahl S, Mogensen M. Structure/performance relations for Ni/yttria-stabilized zirconia anodes for solid oxide fuel cells. *J Electrochem Soc*. 2000;147:475–485.
3. Li C-X, Li C-J, Guo L-J. Effect of composition of NiO/YSZ anode on the polarization characteristics of SOFC fabricated by atmospheric plasma spraying. *Int J Hydrogen Energy*. 2010;35:2964–2969.
4. Ribeiro NFP, Souza MMVM, Macedo Neto OR, Vasconcelos SMR, Schmal M. Investigating the microstructure and catalytic properties of Ni/YSZ cermets as anodes for SOFC applications. *Appl Catal A: Gen*. 2009;353:305–309.
5. Koide H, Someya Y, Yoshida T, Maruyama T. Properties of Ni/YSZ cermet as anode for SOFC. *Solid State Ionics*. 2000;132:253–260.
6. Xia ZT, Chan SH, Khor KA. An improved anode micro-model of SOFC. *Electrochem Solid-State Lett*. 2004;7:A63–A65.
7. Chan SH, Xia ZT. Anode micro-model of solid oxide fuel cell. *J Electrochem Soc*. 2001;148:A388–A394.
8. Costamagna P, Costa P, Antonucci V. Micro-modelling of solid oxide fuel cell electrodes. *Electrochim Acta*. 1998;43:375–394.
9. Jeon DH, Nam JH, Charn-Jung K. Microstructural optimization of anode-supported solid oxide fuel cells by a comprehensive microscale model. *J Electrochem Soc*. 2006;153:A406–A417.

10. Nam JH, Jeon DH. A comprehensive micro-scale model for transport and reaction in intermediate temperature solid oxide fuel cells. *Electrochim Acta*. 2006;51:3446–3460.
11. Farhad S, Hamdullahpur F. Conceptual design of a novel ammonia-fuelled portable solid oxide fuel cell system. *J Power Sources*. 2010;195:3084–3090.
12. Farhad S, Saffar-Avval M, Younessi-Sinaki M. Efficient design of feedwater heaters network in steam power plants using pinch technology and exergy analysis. *Int J Energy Res*. 2007;32:1–11.
13. Farhad S, Younessi-Sinaki M, Golriz MR, Hamdullahpur F. Exergy analysis and performance evaluation of CNG to LNG converting process. *Int J Exergy*. 2008;5:164–176.
14. Sunde S. Monte Carlo simulations of polarization resistance of composite electrodes for solid oxide fuel cells. *J Electrochem Soc*. 1996;143:1930–1939.
15. Ji Y, Yuan K, Chung JN. Monte-Carlo simulation and performance optimization for the cathode microstructure in a solid oxide fuel cell. *J Power Sources*. 2007;165:774–785.
16. Chan SH, Chen XJ, Khor KA. Cathode micromodel of solid oxide fuel cell. *J Electrochem Soc*. 2004;151:A164–A174.
17. Kuo CH, Gupta PK. Rigidity and conductivity percolation thresholds in particulate composites. *Acta Metall Mater*. 1995;43:397–403.
18. Kenney B, Valdmanis M, Baker C, Pharoah JG, Karan K. Computation of TPB length, surface area and pore size from numerical reconstruction of composite solid oxide fuel cell electrodes. *J Power Sources*. 2009;189:1051–1059.
19. Farhad S, Hamdullahpur F. Optimization of the microstructure of porous composite cathodes in solid oxide fuel cells. AIChE Journal, in press, doi: 10.1002/aic.12652.
20. Mason EA. *Gas Transport in Porous Media: The Dusty-Gas Model*. New York: Elsevier, 1983.
21. Hussain MM, Li X, Dincer I. Mathematical modeling of transport phenomena in porous SOFC anodes. *Int J Therm Sci*. 2007;46:48–56.
22. Suwanwarangkul R, Croiset E, Fowler MW, Douglas PL, Entchev E, Douglas MA. Performance comparison of Fick's, dusty-gas and Stefan–Maxwell models to predict the concentration overpotential of a SOFC anode. *J Power Sources*. 2003;122:9–18.
23. Tseronis K, Kookos IK, Therodoropoulos C. Modelling mass transport in solid oxide fuel cell anodes: a case for a multidimensional dusty gas-based model. *Chem Eng Sci*. 2008;63:5626–5638.
24. Gemmen RS, Trembly J. On the mechanisms and behaviour of coal syngas transport and reaction within the anode of a solid oxide fuel cell. *J Power Sources*. 2006;161:1084–1095.
25. Fuller EN, Ensley K, Giddings JC. Diffusion of halogenated hydrocarbons in helium. The effect of structure on collision cross sections. *J Phys Chem*. 1969;73:3679–3685.
26. Chan SH, Khor KA, Xia ZT. A complete polarization model of a solid oxide fuel cell and its sensitivity to the change of cell component thickness. *J Power Sources*. 2001;93:130–140.
27. Poling BE, Prausnitz JM, O'Connell JP. *The Properties of Gases and Liquids*, 5th ed. New York: McGraw-Hill, 2000.
28. Li X. *Principles of Fuel Cells*. New York: Taylor & Francis, 2006.
29. Bard AJ, Faulkner LR. *Electrochemical Methods: Fundamentals and Applications*, 2nd ed. New York: Wiley, 2001.
30. Habibzadeh B. Understanding the CO oxidation in solid oxide fuel cells using nickel patterned anode. PhD thesis, University of Maryland, 2007.
31. Chen XJ, Chan SH, Khor KA. Simulation of a composite cathode in solid oxide fuel cells. *Electrochim Acta*. 2004;49:1851–1861.
32. Farhad S, Yoo Y, Hamdullahpur F. *Performance Evaluation of Different Configurations of Biogas-Fuelled SOFC Micro-CHP Systems for Residential Applications*. Lucerne, Switzerland: European Fuel Cell Forum, 2009.
33. Farhad S, Yoo Y, Hamdullahpur F. *Conceptual Design of Anaerobic Digestion Gas-Fuelled SOFC Systems to Generate Electricity and Heat in Wastewater Treatment Plants*. Newport Beach, California, USA: ASME-ICEPAG, 2009.
34. Farhad S, Hamdullahpur F. Developing fuel map to predict the effect of fuel composition on the maximum voltage of solid oxide fuel cells. *J Power Sources*. 2009;191:407–416.
35. Farhad S, Hamdullahpur F. Developing fuel map to predict the effect of fuel composition on the maximum efficiency of solid oxide fuel cells. *J Power Sources*. 2009;193:632–638.
36. Farhad S, Yoo Y, Hamdullahpur F. Effects of fuel processing methods on industrial scale biogas-fuelled solid oxide fuel cell system for operating in wastewater treatment plants. *J Power Sources*. 2010;195:1446–1453.
37. Farhad S, Hamdullahpur F, Yoo Y. Performance evaluation of different configurations of biogas-fuelled SOFC micro-CHP systems for residential applications. *Int J Hydrogen Energy*. 2010;35:3758–3768.
38. Younessi-Sinaki M, Matida EA, Hamdullahpur F. Kinetic model of homogeneous thermal decomposition of methane and ethane. *Int J Hydrogen Energy*. 2009;34:3710–3716.
39. Younessi-Sinaki M, Matida EA, Hamdullahpur F. Development of a reaction mechanism for predicting hydrogen production from homogeneous decomposition of methane. *Int J Hydrogen Energy*. 2011;36:2936–2944.
40. Song HS, Lee S, Hyun SH, Kim J, Moon J. Compositional influence of LSM–YSZ composite cathodes on improved performance and durability of solid oxide fuel cells. *J Power Sources*. 2009;187:25–31.
41. Song HS, Kim WH, Hyun SH, Moon J, Kimb J, Lee H-W. Effect of starting particulate materials on microstructure and cathodic performance of nanoporous LSM–YSZ composite cathodes. *J Power Sources*. 2007;167:258–264.

Manuscript received Mar. 31, 2011, and revision received May 13, 2011.